On-fiber plasmonic interferometer for multi-parameter sensing

Zhijian Zhang,[1] Yongyao Chen,[1] Haijun Liu,[1,2] Hyungdae Bae,[1] Douglas A. Olson,[2] Ashwani K. Gupta,[1] and Miao Yu[1,*]

[1] *Department of Mechanical Engineering, University of Maryland, College Park, MD 20740,USA*
[2]*National Institute of Standards and Technology, Gaithersburg, MD 20899, USA*
[*]*mmyu@umd.ed*

Abstract: We demonstrate a novel miniature multi-parameter sensing device based on a plasmonic interferometer fabricated on a fiber facet in the optical communication wavelength range. This device enables the coupling between surface plasmon resonance and plasmonic interference in the structure, which are the two essential mechanisms for multi-parameter sensing. We experimentally show that these two mechanisms have distinctive responses to temperature and refractive index, rendering the device the capability of simultaneous temperature and refractive index measurement on an ultra-miniature form factor. A high refractive index sensitivity of 220 nm per refractive index unit (RIU) and a high temperature sensitivity of −60 pm/ °C is achieved with our device.

OCIS codes: (240.6680) Surface plasmons; (260.3160) Interference; (060.4005) Microstructured fibers; (060.2370) Fiber optics sensors.

References and links

1. B. Culshaw, "Optical fiber sensor technologies: opportunities and - perhaps - pitfalls," J. Lightwave Technol. **22**(1), 39–50 (2004).
2. O. S. Wolfbeis, "Fiber-optic chemical sensors and biosensors," Anal. Chem. **80**(12), 4269–4283 (2008).
3. H. Meixner, *Sensors, Micro-and Nanosensor Technology: Trends in Sensor Markets* (John Wiley & Sons, 2008).
4. M. Born and E. Wolf, *Principles of Optics: Electromagnetic Theory of Propagation, Interference and Diffraction of Light* (Cambridge University, 1999).
5. D. K. Gramotnev and S. I. Bozhevolnyi, "Plasmonics beyond the diffraction limit," Nat. Photonics **4**(2), 83–91 (2010).
6. J. Homola, S. S. Yee, and G. Gauglitz, "Surface plasmon resonance sensors: review," Sens. Actuators B Chem. **54**(1-2), 3–15 (1999).
7. K. A. Willets and R. P. Van Duyne, "Localized surface plasmon resonance spectroscopy and sensing," Annu. Rev. Phys. Chem. **58**(1), 267–297 (2007).
8. J. Feng, V. S. Siu, A. Roelke, V. Mehta, S. Y. Rhieu, G. T. R. Palmore, and D. Pacifici, "Nanoscale plasmonic interferometers for multispectral, high-throughput biochemical sensing," Nano Lett. **12**(2), 602–609 (2012).
9. M. Consales, A. Ricciardi, A. Crescitelli, E. Esposito, A. Cutolo, and A. Cusano, "Lab-on-fiber technology: toward multifunctional optical nanoprobes," ACS Nano **6**(4), 3163–3170 (2012).
10. G. Kostovski, P. R. Stoddart, and A. Mitchell, "The optical fiber tip: an inherently light-coupled microscopic platform for micro- and nanotechnologies," Adv. Mater. **26**(23), 3798–3820 (2014).
11. V. Bhatia, "Applications of long-period gratings to single and multi-parameter sensing," Opt. Express **4**(11), 457–466 (1999).
12. O. Frazão, L. A. Ferreira, F. M. Araújo, and J. L. Santos, "Applications of fiber optic grating technology to multi-parameter measurement," Fiber Int. Opt. **24**(3-4), 227–244 (2005).
13. T. Mawatari and D. Nelson, "A multi-parameter Bragg grating fiber optic sensor and triaxial strain measurement," Smart Mater. Struct. **17**(3), 035033 (2008).
14. H. Y. Choi, G. Mudhana, K. S. Park, U.-C. Paek, and B. H. Lee, "Cross-talk free and ultra-compact fiber optic sensor for simultaneous measurement of temperature and refractive index," Opt. Express **18**(1), 141–149 (2010).
15. R. Yang, Y.-S. Yu, C. Chen, Q.-D. Chen, and H.-B. Sun, "Rapid fabrication of microhole array structured optical fibers," Opt. Lett. **36**(19), 3879–3881 (2011).
16. C. Pang, H. Bae, A. Gupta, K. Bryden, and M. Yu, "MEMS Fabry-Perot sensor interrogated by optical system-on-a-chip for simultaneous pressure and temperature sensing," Opt. Express **21**(19), 21829–21839 (2013).
17. C. Chen, Y.-S. Yu, X.-Y. Zhang, R. Yang, C.-C. Zhu, C. Wang, Y. Xue, F. Zhu, Q.-D. Chen, and H.-B. Sun, "Compact fiber tip modal interferometer for high-temperature and transverse load measurements," Opt. Lett. **38**(17), 3202–3204 (2013).

18. D. J. Hu, J. L. Lim, M. Jiang, Y. Wang, F. Luan, P. P. Shum, H. Wei, and W. Tong, "Long period grating cascaded to photonic crystal fiber modal interferometer for simultaneous measurement of temperature and refractive index," Opt. Lett. **37**(12), 2283–2285 (2012).
19. H.-J. van Manen, P. Verkuijlen, P. Wittendorp, V. Subramaniam, T. K. van den Berg, D. Roos, and C. Otto, "Refractive index sensing of green fluorescent proteins in living cells using fluorescence lifetime imaging microscopy," Biophys. J. **94**(8), L67–L69 (2008).
20. H. Liao, C. L. Nehl, and J. H. Hafner, "Biomedical applications of plasmon resonant metal nanoparticles," Nanomedicine (Lond) **1**(2), 201–208 (2006).
21. Disclaimer: Certrain commercial equipment, instruments, materials, or software are identified in this paper to foster understanding. Such identification does not imply endorsement by NIST, nor does it imply that the items or software identified are necessarily the best available for the purpose.
22. F. Miyamaru and M. Hangyo, "Finite size effect of transmission property for metal hole arrays in subterahertz region," Appl. Phys. Lett. **84**(15), 2742–2744 (2004).
23. J. A. Sánchez-Gil and A. A. Maradudin, "Surface-plasmon polariton scattering from a finite array of nanogrooves/ridges: efficient mirrors," Appl. Phys. Lett. **86**(25), 251106 (2005).
24. Z. M. Zhang, *Nano/microscale Heat Transfer* (McGraw-Hill, 2007).
25. J. B. Pendry, L. Martín-Moreno, and F. J. Garcia-Vidal, "Mimicking Surface Plasmons with Structured Surfaces," Science **305**(5685), 847–848 (2004).
26. P. B. Catrysse, G. Veronis, H. Shin, J.-T. Shen, and S. Fan, "Guided modes supported by plasmonic films with a periodic arrangement of subwavelength slits," Appl. Phys. Lett. **88**(3), 031101 (2006).
27. S. H. Mousavi, A. B. Khanikaev, B. Neuner 3rd, Y. Avitzour, D. Korobkin, G. Ferro, and G. Shvets, "Highly Confined Hybrid Spoof Surface Plasmons In Ultrathin Metal-Dielectric Heterostructures," Phys. Rev. Lett. **105**(17), 176803 (2010).
28. H. F. Schouten, N. Kuzmin, G. Dubois, T. D. Visser, G. Gbur, P. F. A. Alkemade, H. Blok, G. W. Hooft, D. Lenstra, and E. R. Eliel, "Plasmon-assisted two-slit transmission: Young's experiment revisited," Phys. Rev. Lett. **94**(5), 053901 (2005).
29. F. López-Tejeira, S. G. Rodrigo, L. Martin-Moreno, F. J. Garcia-Vidal, E. Devaux, T. W. Ebbesen, J. R. Krenn, I. P. Radko, S. I. Bozhevolnyi, M. U. Gonzalez, J. C. Weeber, and A. Dereux, "Efficient unidirectional nanoslit couplers for surface plasmons," Nat. Phys. **3**(5), 324–328 (2007).
30. Y.-W. Jiang, L. D. Tzuang, Y.-H. Ye, Y.-T. Wu, M.-W. Tsai, C.-Y. Chen, and S.-C. Lee, "Effect of Wood's anomalies on the profile of extraordinary transmission spectra through metal periodic arrays of rectangular subwavelength holes with different aspect ratio," Opt. Express **17**(4), 2631–2637 (2009).
31. B. N. Taylor, *Guidelines for Evaluating and Expressing the Uncertainty of NIST Measurement Results* (DIANE Publishing, 2009).
32. B. Qi, G. R. Pickrell, J. Xu, P. Zhang, Y. Duan, W. Peng, Z. Huang, W. Huo, H. Xiao, R. G. May, and A. Wang, "Novel data processing techniques for dispersive white light interferometer," Opt. Eng. **42**(11), 3165–3171 (2003).
33. J. Park and B. Lee, "An approximate formula of the effective refractive index of the metal–insulator–metal surface plasmon polariton waveguide in the infrared region," Jpn. J. Appl. Phys. **47**(11), 8449–8451 (2008).
34. S. Tripura Sundari, K. Srinivasu, S. Dash, and A. Tyagi, "Temperature evolution of optical constants and their tuning in silver," Solid State Commun. **167**, 36–39 (2013).
35. D. B. Leviton and B. J. Frey, "Temperature-dependent absolute refractive index measurements of synthetic fused silica," in *Astronomical Telescopes and Instrumentation* (International Society for Optics and Photonics, 2006), pp. 62732K–62732K–62711.
36. G. White and J. Collins, "Thermal expansion of copper, silver, and gold at low temperatures," J. Low Temp. Phys. **7**(1-2), 43–75 (1972).
37. Y. Fei, "Thermal expansion," AGU Ref. Shelf **2**, 29–44 (1995).
38. S. J. Mihailov, "Fiber Bragg grating sensors for harsh environments," Sensors (Basel) **12**(2), 1898–1918 (2012).

1. Introduction

For decades, sensor miniaturization has received a lot of attention in a broad range of applications for physical, chemical and biomedical parameters sensing [1, 2]. Owing to the recent advances in micro/nano fabrication techniques [3], miniature sensors can be realized in smaller and smaller scales. As a popular miniature sensor platform, optical fiber based sensors have been extensively investigated because of their small sizes, light weight, flexibility, robustness to electromagnetic interference, and remote sensing ability [1]. However, as the size of a conventional optical element gets closer to the operating wavelength, the size of fiber-optic sensors seems irreducible due to the diffraction limit [4], Nevertheless, recent studies on surface plasmons (SPs) shed some light on the realization of optical devices with an even smaller form factor. SPs are electromagnetic wave induced collective oscillations of free electrons on a metal/dielectric interface with a wavelength shorter than that of the incident light, which enable the confinement and manipulation of light at the subwavelength scale [5]. With the help of SPs, sensors with excellent sensing ability and ultra-thin film configurations have been demonstrated, including SP resonance [6], localized SP [7], and plasmonic interferometer based sensors [8]. Recently, the facet of an optical fiber tip is found to be an appealing platform to integrate plasmonic structures for sensing applications [9, 10]. However, all of these sensors are either limited to single parameter sensing or can be sensitive to multiple parameters but are not capable of distinguishing different parameters.

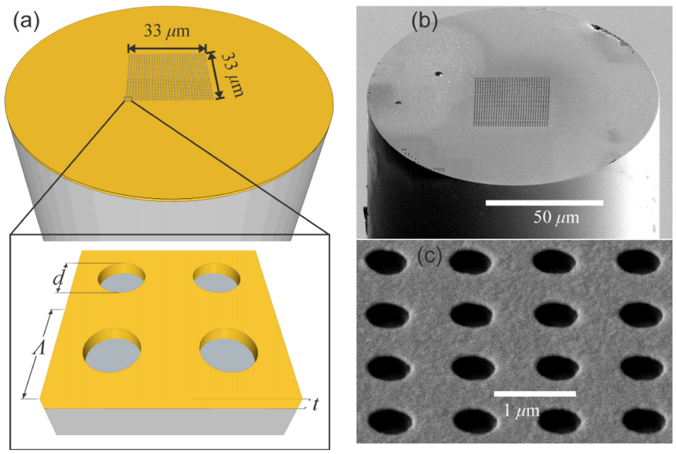

Fig. 1. (a) Schematic of on-fiber plasmonic interferometer with nano-hole array. The inset shows the unit cells of the array (t = 150 nm, d = 528 nm and Λ = 1055 nm). (b) SEM of the fabricated sensor. (c) SEM of the nano-hole array.

On the other hand, sensors with multi-parameter sensing ability become more and more important, since in practical situations the measured parameters are often coupled with each other. Therefore, sensor designs that can distinguish different parameters in a single measurement are highly desirable. Over the last decade, a number of multi-parameter fiber-optic sensors have been presented [11–18]. There are generally two methods. One method is to include additional sensing elements to measure different parameters, such as dual Bragg gratings in a fiber [13], cascaded Fabry–Pérot (FP) cavities [14, 16], and fiber Bragg grating (FBG) cascaded to a photonic crystal fiber interferometer [18]. Consequently, this method will increase the size of the sensor. Another method is to utilize multiple modes that are distinctively responsive to different parameters. As a result, multiple parameters can be discriminated by using a sensitivity matrix [12, 15–17]. However, all these sensors utilize conventional optical components with a relatively large sensor size.

In this paper, we present a novel miniature on-fiber multi-parameter sensor based on a plasmonic interferometer. The sensor consists of a two-dimensional (2D) nano-hole array pattern fabricated on a silver film deposited on a cleaved fiber facet, as shown in Fig. 1. The nano-hole array induces SPs, which propagate at the interface of metal and silica, resulting in plasmonic interference of the multiple reflections at the boundaries of the finite-sized pattern. Owing to the distinct responses of the SP resonance and the plasmonic interference to temperature and refractive index, simultaneous measurements of temperature and refractive index can be achieved, which are the essential sensing parameters in many biomedical applications [19, 20].

2. Fabrication and experiment

To fabricate the on-fiber plasmonic interferometer illustrated in Fig. 1(a), a single mode fiber (SMF28, Corning) [21] was first cleaved with a typical cleave angle of ± 0.5°. Next, a silver film with a thickness of t = 150 nm was deposited on the cleaved facet by magnetron sputtering. Further, a focused ion beam (FIB) (Helios 650, FEI) milling was used to write the nano-hole array pattern on the silver film around the fiber core region. The diameter d of the individual hole was designed to be 528 nm and periodicity Λ is 1055 nm. The entire array pattern consists of 31 × 31 units with an overall patterned area of d × d (≈33 μm × 33 μm).

#233806 - $15.00 USD Received 6 Feb 2015; revised 25 Mar 2015; accepted 2 Apr 2015; published 16 Apr 2015

This design ensures the following: i) SPs can be excited around the optical communication wavelength of 1550 nm, ii) a proper free spectrum range is obtained to observe multiple fringes in our spectrum range, iii) the SP resonance will not be degraded by the finite pattern size [22, 23], and iv) the entire core area of the fiber is covered by the hole array. The scanning electron microscopy (SEM) pictures of the fabricated device are shown in Figs. 1 (b) and 1(c).

The reflection spectrum of the fabricated device was measured by using an optical sensing interrogator (SM130, Micron Optics) with an uncertainty of 1 pm in the wavelength range from 1510 nm to 1590 nm. The remote sensing configuration was used, so that both incident light and the reflected signal can be guided through the fiber, as shown in Fig. 2(a). A polarization controller was used in the light path to control the light polarization. The measured reflection spectra were normalized by the reflection spectrum of a fixed fiber mirror (a cleaved fiber with 150 nm silver deposited without patterning). Note that the nano-hole array structure was designed to be polarization independent, since the 2D symmetric structure is illuminated under normal incidence through the fiber. A typical reflection spectrum of the sensor is shown in Fig. 2(b), which is a result of two mechanisms: SP resonance and plasmonic interference. The incident light first interacts with the hole-array structure. Due to the grating diffraction of the nanopattern, momentum matching can be achieved, which leads to effective coupling from incident light to SPs at the resonant wavelength [24]:

$$\lambda_{resonace} = \Lambda\sqrt{\frac{\varepsilon_d(\lambda)\varepsilon_m(\lambda)}{\varepsilon_d(\lambda)+\varepsilon_m(\lambda)}}, \tag{1}$$

where ε_d and ε_m are the permittivities of silica (or environment media) and silver, respectively. It should be noted that SP resonance is usually accompanied with Wood's anomalies in long wavelength region [30]. The Wood's anomaly happens at the wavelength predicted by $\lambda_{Wood's} = \Lambda\sqrt{\varepsilon_d(\lambda)}$, which is close to the SP resonance but at a shorter wavelength. Moreover, the individual holes can act as elementary scatters, enabling broadband excitation of surface waves [see Fig. 2(e)] that resemble the spoof/hybrid surface plasmons (SSPs) [25–27] counter-propagating on the hole-array structures. These surface modes will be reflected at the boundaries of the hole-array pattern, resulting in an interference effect of surface waves propagating at the metal-fiber interface. It should be noted that the SSPs can be re-scattered through the individual holes, and the re-scattered signals can be collected and guided through the optical fiber. From the fringe pattern shown in the fiber reflection spectrum [Fig. 2(b)], it indicates that the interference effect of SSPs on the fiber end-face can be measured and characterized in the far field. Therefore, the sensor can act as a plasmonic interferometer [8, 28, 29] as well as a SP resonator.

To clearly observe the two different mechanisms from the reflection spectrum, fast Fourier transform (FFT) of the measured spectrum is performed and the corresponding spatial frequency spectrum (i.e., wavenumber spectrum) is obtained [14, 17]. It is noted that the SP resonance mainly affects the low spatial frequency components while the plasmonic interference contributes to the higher spatial frequency components of the spatial frequency spectrum. After filtering out the direct current (DC) component in the spatial frequency spectrum, two bandpass filters were applied to the first and second peaks of the spatial frequency spectrum, and then inverse FFT was performed to the two filtered spectra respectively. Therefore, two distinctive spectra corresponding to the SP resonance effect [Fig. 2(c)] and plasmonic interference [Fig. 2(d)] can be obtained. Figure 2(c) shows an asymmetric Fano line shape of the spectrum, which clearly indicates a SP resonance peak accompanied by a Wood's anomaly dip at a shorter wavelength. On the other hand, Fig. 2(d) clearly indicates the periodic fringes of a F-P interferometer due to the plasmonic interference. To validate the influence of SP resonance, a rigorous coupled-wave analysis (RCWA) simulation was conducted for a nano-hole array structure with the same hole diameter and periodicity as the fabricated device but an infinite size, shown in Fig. 2(f). Due

#233806 - $15.00 USD Received 6 Feb 2015; revised 25 Mar 2015; accepted 2 Apr 2015; published 16 Apr 2015

to the excitation of SPs, a resonance peak can be found around 1553 nm in the reflection spectrum, which agrees well with the theoretical prediction using Eq. (1) (≈1542 nm). Further, it can be seen that the spectrum obtained with RCWA simulations exhibits an asymmetric Fano line shape, which matches with the filtered experimental spectrum shown in Fig. 2(b). The experimentally measured resonance peak is about 1558 nm, which agrees well with the theoretical prediction and numerical simulation.

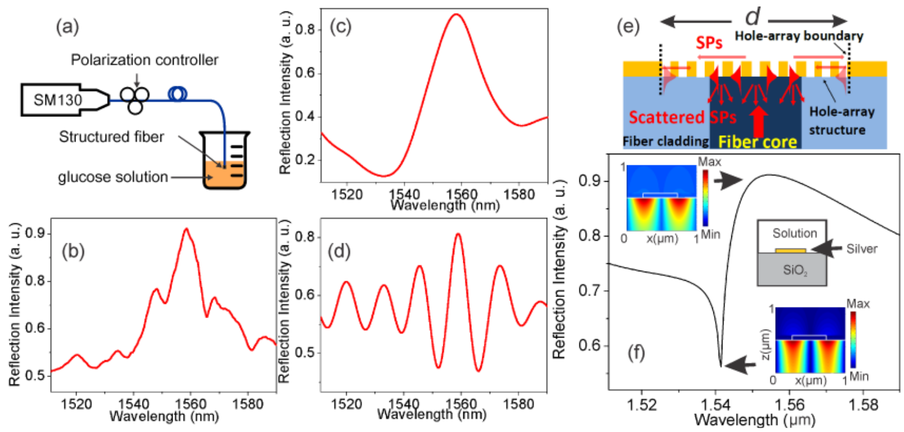

Fig. 2. (a) Schematic of the experimental setup, (b) typical reflection spectrum of the sensor in glucose solution at room temperature (glucose concentration 10%), (c) reflection spectrum of SP resonance extracted from (b), (d) reflection spectrum of plasmonic interference extracted from (b), (e) The schematic of the on-fiber plasmonic interference effect, and (f) reflection spectrum obtained with RCWA simulations for a hole array structure of infinite size in a 10% glucose solution. The insets show the field distributions at the SP resonance peak and the Wood's anomaly dip in one unit cell.

To demonstrate the multi-parameter sensing ability of the on-fiber plasmonic interferometer, the responses of the sensor was characterized with respect to refractive index of the environment and temperature changes. In the refractive index experiments, the sensor was immersed in glucose/water solution. By changing the concentration of glucose solution to 5%, 10%, 15%, 20%, and 25%, the refractive index of the solution was tuned to 1.3382, 1.3448, 1.3506, 1.3575 and 1.3623 respectively. The refractive index of the solution was calibrated by using a refractometer (Digital Brix/RI-Chek, Reichert) with an uncertainty of 4.1×10^{-5} (note the uncertainties discussed in this paper are defined by the coverage factor k = 1 [31]). The temperature measurements were conducted in air by using a temperature control chamber that allows us to accurately calibrate temperature. The device was sandwiched between two polyimide-insulated flexible film heaters (KH 103/10, Omega Engineering Inc.) and the temperature control was achieved by using a temperature controller (CN77333, Omega Engineering Inc.) with a film thermocouple (CO1-K, Omega Engineering Inc.) as the reference that has a measurement uncertainty of 0.4 °C.

Further, the spatial frequency filtering method was used to extract the spectra dominated by two different mechanisms discussed previously. For refractive index measurements, Fig. 3(a) shows the filtered spectra dominated by the SP resonance. The SP resonance exhibits a red shift with increasing refractive index of the solution, which is consistent with the prediction of Eq. (1). By tracing the shift of SP resonance, the refractive index of the solution can be determined. Here, the Wood's anomaly dip was not used to obtain the refractive index change. Instead, the SP resonance peak was chosen, since it is more sensitive to the refractive index change. This can be explained by using the field distributions obtained at the SP resonance peak and the Wood's anomaly dip [insets of Fig. 2(f)]. At the Wood's anomaly, light is mostly confined in the SiO_2 region, while around the SP resonance more evanescent field can extend into the environment (solution region), hence the SP peak is more sensitive to the environmental changes. Figure 3 (b) shows the obtained peak wavelength shift with respect to the refractive index change. The estimated sensitivity is 220 nm/RIU with an uncertainty of 2.1%. All the sensitivity uncertainties calculated here are standard deviations based on the linear fits. Similarly, the high spatial frequency contribution from plasmonic interference was extracted [see Fig. 3(c)]. By tracking the peak around 1545 nm, the effective optical path difference (OPD) for the interference was obtained by using the one peak tracing method [32] [see Fig. 3(d)]. The effective OPD increases with increasing the refractive index. The sensitivity of effective OPD with respect to the refractive index change of the environment was determined to be 1700 nm/RIU with an uncertainty of 17.2%. It should be noted that a linear fit was used in Fig. 3(d) because of the underlying mechanism. It is known that OPD = $2n_{eff}d$, where d is the pattern size and n_{eff} is effective refractive index of surface plasmon modes on the hole-array structure. Since the effective refractive index is proportional to the environmental dielectric refractive index in the infrared region ($n_{eff} \propto \sqrt{\varepsilon_d}$) [33], the effective OPD should change linearly with respect to the environment refractive index change. However, due to the short wavelength span (80 nm) of the interrogator (SM130) used in the experiment, the resolution of the obtained spatial frequency spectra was limited. This is believed to cause the relatively large deviations of the experimental data from the linear fit in Fig. 3(d).

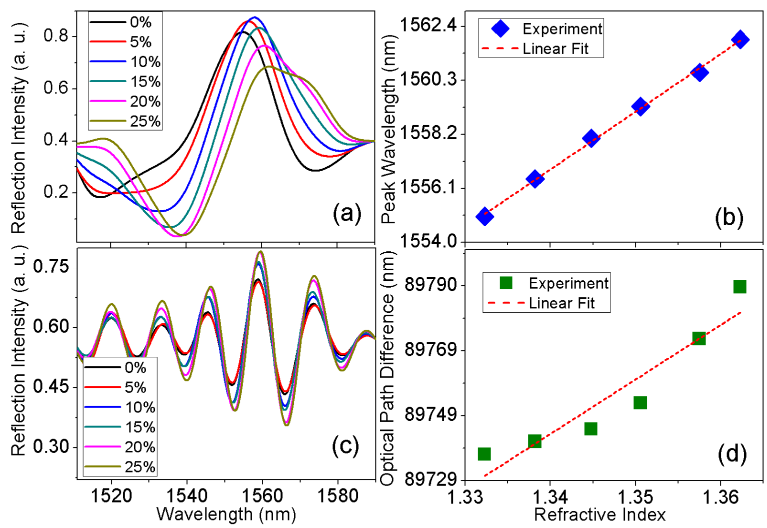

Fig. 3. (a) Extracted reflection spectra dominated by SP resonance with respect to refractive index change, (b) peak wavelength of the SP resonance versus refractive index, (c) extracted reflection spectra dominated by plasmonic interference with respect to different refractive indices, (d) effective OPD versus refractive index.

With the spatial frequency filtering method, the spectra obtained at different temperatures in air were also analyzed [see Fig. 4]. As shown in Figs. 4(a) and 4(b), the peak wavelength due to the SP resonance manifests a blue shift as the temperature increases. This is because the negative thermo-optical coefficient of silver (on the order of 10^{-3}/°C around 1550 nm [34]) dominates in the temperature measurement, compared with the thermo-optical coefficient of SiO_2 (on the order of 10^{-6}/°C [35]) and thermal expansion coefficient of both silver and SiO_2 (on the order of 10^{-6}/°C [36, 37]). The temperature sensitivity of the SP resonance was obtained as −60 pm/°C with an uncertainty of 11.6%. Furthermore, the effective OPD increases as the temperature rises [see Figs. 4(c) and 4(d)]. The temperature sensitivity for the effective OPD was estimated to be 500 pm/ °C with an uncertainty of 9.7%.

In order to distinguish the refractive index and temperature in a single measurement, the sensitivity matrix method was used, in which the refractive index and temperature changes (Δn, ΔT) as functions of the peak wavelength shift of the SP resonance and the effective OPD change ($\Delta\lambda$, ΔL) can be represented as

#233806 - $15.00 USD Received 6 Feb 2015; revised 25 Mar 2015; accepted 2 Apr 2015; published 16 Apr 2015

$$\begin{pmatrix}\Delta n\\ \Delta T\end{pmatrix} = K^{-1}\begin{pmatrix}\Delta\lambda\\ \Delta L\end{pmatrix} = \begin{pmatrix}k_{\lambda,n} & k_{\lambda,T}\\ k_{L,n} & k_{L,T}\end{pmatrix}^{-1}\begin{pmatrix}\Delta\lambda\\ \Delta L\end{pmatrix} = \begin{pmatrix}220nm/RIU & -60\times10^{-3}nm/^{\circ}\mathrm{C}\\ 1700nm/RIU & 500\times10^{-3}nm/^{\circ}\mathrm{C}\end{pmatrix}^{-1}\begin{pmatrix}\Delta\lambda\\ \Delta L\end{pmatrix}, \tag{2}$$

where K is the sensitivity matrix, $k_{\lambda,n}$ and $k_{L,n}$ are the refractive index sensitivities of SP resonance peak and the effective OPD, respectively, and $k_{\lambda,T}$ and $k_{L,T}$ are the corresponding temperature sensitivities, respectively.

Note that the $k_{L,n}$, $k_{L,T}$ are obtained only for facilitating the multi-parameter sensing and discriminating the temperature and refractive index change. In terms of wavelength shift, the SP resonance gives much larger sensitivities as the primary system sensitivities for refractive index and temperature measurements. For the SP resonance, the obtained refractive index sensitivity of 220 nm/RIU is comparable to the localized SP sensor on a fiber facet working in the visible region [9]. Moreover, the temperature sensitivity of −60 pm/°C is six times higher than that of a FBG temperature sensor [38].

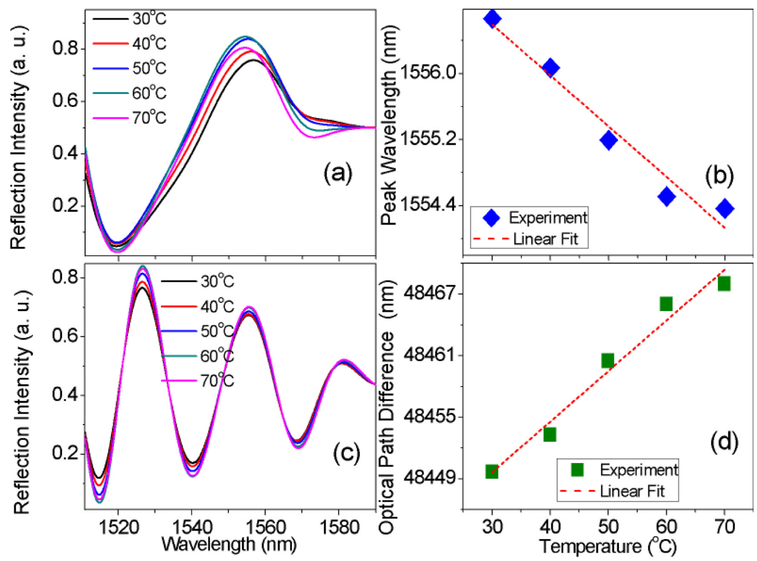

Fig. 4. (a) Extracted reflection spectra dominated by SP resonance with respect to temperature change, (b) peak wavelength of SP resonance versus temperature, (c) extracted reflection spectra due to plasmonic interference with respect to temperature change, and (d) effective OPD versus temperature.

3. Discussion

The geometries of the hole-array structure can play an important role to modify the SP dispersion relation, and therefore can influence the plasmonic interference effect. The fringe pattern appears in the reflection spectrum [see Fig. 2(d)] clearly indicates the interference effect of SPs, which may be characterized by an effective F-P resonance equation:

$$k_{sp}(\omega)\cdot d - 2\varphi(\omega) = m\pi. \tag{3}$$

Here, $k_{sp}(\omega)$ is the wave-vector of the SPs and $\varphi(\omega)$ represents the phase shift due to the SPs reflection at the boundaries of the hole-array structure. m is a positive integer corresponding to the F-P mode orders (i.e., m = 1, 2, ...). Since the SPs are re-scattered at the fiber-hole array interface, the far-field measurement of the spectrum fringe pattern will carry the information about the SPs modes, and the dispersion relation of the SPs may be extracted from the fringe pattern of the reflection spectrum by using the following approximations:

$$d(2\pi/\lambda_i)n_i - 2\varphi_i = (m+i)\cdot\pi, \tag{4}$$

where i = 1,2,3... represents the order of the fringe pattern shown in Fig. 2(d), λ_i is the mode wavelength corresponding to the fringe peaks in the reflection spectrum (counted from long wavelength to short wavelength), and n_i is the effective refractive index of the SPs. For closely spaced fringes in the spectrum, the phase-shift difference between these modes (e.g., i and i + 1) is assumed to be small so that $\varphi_i \approx \varphi_{i+1}$ .On the other hand, since the SPs with larger wavelength will be relatively insensitive to the surface patterns, the SPs on the hole array in the long wavelength region (e.g., λ_1 = 1587.5 nm) may behave as a surface plasmon mode propagating on a flat metal surface, and approximately satisfy the relation $n_1 \approx n_{sp} = \sqrt{\varepsilon_m \varepsilon_d/(\varepsilon_m + \varepsilon_d)}$. Based on the Eq. (4) and the above approximations, the effective refractive index n_i of the SPs can be estimated from the fringing patterns obtained from the experimental measurements as

$$n_{i+1} = \lambda_{i+1}/2d + n_i\lambda_{i+1}/\lambda_i, \tag{5}$$

and the dispersion relations of the SPs can be obtained as

$$k(f_i) = n_i\, 2\pi/\lambda_i, \tag{6}$$

where f_i corresponds to the frequency of SPs. As shown in Fig. 5, in the low frequency region, the dispersion curve of SPs on the hole-array structure approaches the dispersion line of SPs on the flat silver surface, while at high frequency region it starts to derivate from that of the flat silver surface. Therefore, it is evident from the experiment that the hole-array structure will modify the dispersion properties of SPs as compared with SPs propagating on a flat metal surface, which is due to the spoof or hybrid surface plasmons supported by the hole-array structures [25–27]. The reflection of SPs at the boundaries of the hole-array pattern is due to the wave impedance mismatch (i.e., refractive index difference) in the hole-array region and outside the hole-array pattern. It is expected that the geometries of the hole-array structure, including the size, shape, and depth of the individual holes as well as the periodicity of the array can modify the dispersion relation of the SPs [27], and therefore will influence the effective F-P resonance due to the plasmonic interference effect.

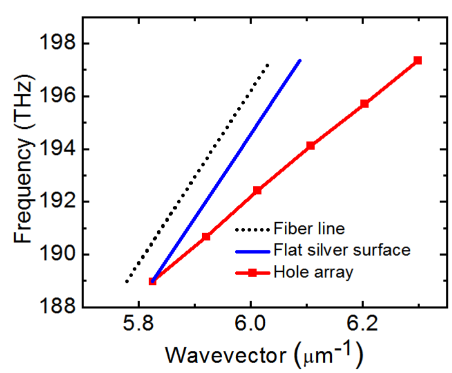

Fig. 5. The comparison of dispersion relations of surface plasmons on the hole array structure (red line) and on the flat silver surface (blue line). The dashed line represents the light dispersion in the fiber core region.

It should be noted that although the above analytical model can provide a good physical understanding of the on-fiber plasmonic interference effect, it cannot be used to accurately characterize the influences of hole-array geometries on the free-spectrum-range (FSR) and finesse of the plasmonic F-P cavity. These comprehensive characterizations and analyses require more rigorous numerical simulations (e.g., three-dimensional FDTD simulations), which is beyond the scope of this work.

4. Conclusion

In conclusion, an on-fiber plasmonic interferometer with nanohole array structures has been successfully demonstrated for multi-parameter sensing. This device can excite SPs in the optical communication wavelength range and induce plasmonic interference due to the finite pattern area. The influences of two different mechanisms (i.e., SP resonance and plasmonic interference) on the reflection spectrum have been studied and utilized as a novel mechanism for multi-parameter sensing on a miniaturized sensing area. To the best of our knowledge, this is the first time that high sensitivity, simultaneous sensing of refractive index (220 nm/RIU) and temperature (−60 pm/ °C) has been achieved by using such a compact device. Owing to the ultra-thin sensing element (≈150 nm thick) with a small sensing area (≈33 μm × 33 μm), our sensor has a much smaller volume than conventional fiber optic sensors. Moreover, the sensing is based on the measurement of SPP evanescent fields, thus enabling a very short light-sample interaction depth of about 1 μm. This enables the capability of measuring the refractive index of femto-liter samples (≈33 μm × 33 μm × 1 μm) and at the same time provides a high spatial resolution for temperature sensing. This work renders a new paradigm for the realization of ultra-miniature multi-parameter optical sensors, which can impact many fronts, such as biological and chemical sensing, biomedical diagnostic, and environmental sensing.

Acknowledgments

This work is partially supported by Office of Naval Research (ONR) High-Temperature Energy Systems (HiTES) Program, US Department of Energy (DOE), and National Institute of Standard and Technology (NIST) (70NANB12H21).